JOURNAL OF COMPUTATIONAL PHYSICS 79, 209–226 (1988)

Macroscale Implicit Electromagnetic Particle Simulation of Magnetized Plasmas

MOTOHIKO TANAKA

Institute for Fusion Theory, Hiroshima University
Hiroshima 730, Japan

Received October 25, 1985; revised January 8, 1988

An electromagnetic and multi-dimensional macroscale particle simulation code (MACROS) is presented which enables us a large time and spatial scale kinetic simulation of magnetized plasmas. Particle ions, finite mass electrons with the guiding-center approximation, and a complete set of Maxwell equations are employed. Implicit field–particle coupled equations are derived in which a time-decentered (slightly backward) finite differential scheme is used to achieve stability for large time and spatial scales. It is shown analytically that the present simulation scheme suppresses high frequency electromagnetic waves and that it accurately reproduces low frequency waves in the plasma. These properties are verified by numerical examination of eigenmodes in a 2D thermal equilibrium plasma and by that of the kinetic Alfven wave.

1. INTRODUCTION

There is a wide variety of physics problems that have MHD time and spatial scales yet showing kinetic natures. For example, an intense electron beam injected into a magnetized plasma is subject to kink instability [1], but this transient behavior cannot be treated by the MHD simulation code because of multi-valued particle velocity distribution and divergence of the current density especially at the beam front. Another example is a propagation of the kinetic Alfven wave [2] which has an MHD wavelength along the ambient magnetic field while wave-particle interactions are essential due to finite ion Larmor radius effect.

If an explicit particle code is adopted to these studies, one is bound by strong restrictions on the spatial length and time scales. These restrictions are $\Delta x < \lambda_e$ and $\omega_{pe} \Delta t < 1$, where Δx is the grid spacing, Δt is the time step, λ_e is the Debye length and $\omega_{pe} = (4\pi n e^2/m_e)^{1/2}$ is the electron plasma frequency [3]. Many efforts have been made in the past to relax these restrictions imposed on the conventional particle code. The *implicit moment method* which was proposed by Mason [4] and Denavit [5] in analogy to the fluid calculations utilizes a time-decentering and some prediction technique for the future velocity moments. This method was successfully implemented for two-dimensional electromagnetic plasma simulations (the *Venus Code* [6, 7]). The other type of implicit simulation model which is

0021-9991/88 $3.00

called the *direct implicit method* introduces to the equation of motion a time low-pass filter on the basis of linear analysis of wave stability [8, 9]. An electromagnetic version of this method was also implemented [10, 11]. So far, however, an inhomogeneity of the plasma has not been included in these models for $\omega_{ce} \Delta t \gg 1$ case, where ω_{ce} is the electron cyclotron frequency.

The Macroscale Particle Simulation Code (MACROS) to be described in this paper has been developed in a phylosophy such that its numerical properties are transparent even in highly nonlinear regimes and that the inhomogeneity effects are easily to be incorporated in the simulation code. The first point has been realized by introducing a *time-decentered* (slightly backward) discretization technique both into the equations of motion and the Maxwell equations [12, 13]. These equations are combined to yield fully implicit field–particle coupled equations. The second point is to be achieved by adding implicit source terms to the field-particle coupled equations. The present scheme brings forth an artificial, almost pure damping of high frequency waves with $\omega \Delta t > 1$, where ω is the characteristic frequency of the wave. An introduction of the artificial damping of high-frequency waves by modifying the Maxwell (field) equations is similar to the moment implicit method [6]. A major difference of the moment method and the present method is the way to predict the current and charge densities of the future time level. In the MACROS code, the current and charge densities are expressed as direct sums of particle and field quantities.

To summarize, the *macroscale particle simulation code* has the features of both the magnetohydrodynamic (MHD) fluid code and the particle code. However, MACROS code includes a large scale electrostatic potential field and the response of the electrons to slowly varying fields; the ion finite Larmor radius effects are also retained. Therefore, the MACROS code is applicable to simulations of large (MHD) scale, nonlinear plasma phenomena where the kinetic effects are essential.

In Section 2 of this paper, methodology and implementation of the macroscale particle simulation code are to be described. Linear stability of this scheme will be analytically shown in Section 3. Section 4 will be dedicated to numerical examples to verify the present simulation scheme; electromagnetic eigenmodes in a two-dimensional magnetized plasma will be shown. A propagation and Landau damping of the finite amplitude kinetic Alfven wave will then be demonstrated. Section 5 will be a summary and conclusion of this paper. Some comments on the application of the macroscale particle simulation code will also be given in this section.

2. Methodology of Macroscale Particle Simulation (MACROS)

The present simulation code uses super-particles for all the species consisting of the plasma. An advantage of using particle electrons with the finite mass is a capability of treating electron transport along/across the magnetic field in response to the global scale electric and magnetic fields [1, 2, 13]. The motion of electrons,

such as the $E \times B$ drift, magnetic drifts under the guiding center approximation, is naturally incorporated in the simulation code.

The equations of motion for the ions are

$$\begin{aligned} d\mathbf{v}_j^{n+1/2}/dt &= (e_i/m_i)[\mathbf{E}^{n+\alpha}(\mathbf{x}_j) + (\mathbf{v}_j^{n+1/2}/c) \times \mathbf{B}^{n+\alpha}(\mathbf{x}_j)], \\ d\mathbf{x}_j^{n+1/2}/dt &= \mathbf{v}_j^{n+1/2}, \end{aligned} \tag{1}$$

where, $\mathbf{x}_j$, $\mathbf{v}_j$ are, respectively, the position and velocity of the jth ions; e_i and m_i are, respectively, their charge and mass; c is the speed of light; $\mathbf{E}$ and $\mathbf{B}$ are the electric and magnetic field, respectively. It is noted in Eq. (1) that the electric and magnetic fields are those at the intermediate time level $(n+\alpha)$, where α $(\alpha > \frac{1}{2})$ is a decentering parameter.

For the electrons, the parallel motion is treated in the same way as the ions; the guiding center approximation is used for the perpendicular motion:

$$\begin{aligned} d\mathbf{v}_\parallel^{n+1/2}/dt &= (e/m_e)\, \mathbf{E}_\parallel^{n+\alpha}(\mathbf{x}_j), \qquad \mathbf{v}_\perp^{n+\gamma} = c(\mathbf{E} \times \mathbf{B}/B^2)^{n+\gamma}\,(\mathbf{x}_j), \\ d\mathbf{x}_j^{n+1/2}/dt &= (\mathbf{v}_\parallel^{n+1/2} + \mathbf{v}_\perp^{n+\gamma}). \end{aligned} \tag{2}$$

The decentering parameters α, γ are both in the range $\frac{1}{2} < \alpha, \gamma < 1$. In Eq. (2), the decentering of the perpendicular velocity has an effect of suppressing unstable cross-field drift motion (see Section 3 for the analysis). We can also use Eq. (1) for the electrons if we study phenomena whose characteristic frequency is less than ω_{ce}. Even in this case, we can have $\Delta x \gg \lambda_e$ and $\omega_{pe}\Delta t \gg 1$ with a use of the following field equations.

Equations (1) and (2) are time-discretized in the following manner:

$$\begin{aligned} \mathbf{v}^{n+1} &= \mathbf{v}^n + \Delta t(e_i/m_i)[\mathbf{E}^{n+\alpha}(\tilde{\mathbf{x}}^{n+\gamma}) + (\mathbf{v}^{n+1/2}/c) \times \mathbf{B}^{n+\alpha}(\tilde{\mathbf{x}}^{n+\gamma})], \\ \mathbf{x}^{n+1} &= \mathbf{x}^n + \Delta t\, \mathbf{v}^{n+1/2} \end{aligned} \tag{3}$$

for the ions, and

$$\begin{aligned} \mathbf{v}_\parallel^{n+1} &= \mathbf{v}_\parallel^n + \Delta t(e/m_e)\, \mathbf{E}_\parallel^{n+\alpha}(\tilde{\mathbf{x}}^{n+\gamma}), \\ \mathbf{x}^{n+1} &= \mathbf{x}^n + \Delta t[\mathbf{v}_\parallel^{n+1/2} + \mathbf{v}_\perp^{n+\gamma}(\tilde{\mathbf{x}}^{n+\gamma})] \end{aligned} \tag{4}$$

for the electrons (the particle number index j has been suppressed in Eqs. (3) and (4)). The particle position and velocity are defined on the same integer time level. The fields $\mathbf{E}^{n+\alpha}$, $\mathbf{B}^{n+\alpha}$ are evaluated at the *known* future particle position $\tilde{\mathbf{x}}^{n+\gamma} = \mathbf{x}^n + \gamma \Delta t\, \mathbf{v}^n$. For extension of the guiding center motion of the electrons, $-\mu \nabla B$, $\mathbf{v}_{\nabla B} \cdots$ terms are to be added as implicit terms to the equations of motion and the field equations assuming that the magnetic moment $\mu = (\frac{1}{2})\, m_e \mathbf{v}_\perp^2/B_0 =$ invariant.

For the electromagnetic fields, a complete set of the Maxwell equations is used which can be coded in a time marching fashion:

$$\frac{1}{c}\frac{\partial \mathbf{B}}{\partial t} = -\nabla \times \mathbf{E},$$

$$\frac{1}{c}\frac{\partial \mathbf{E}}{\partial t} = \nabla \times \mathbf{B} - \frac{4\pi}{c}\mathbf{j}, \tag{5}$$

$$\nabla \cdot \mathbf{E} = 4\pi q, \qquad \nabla \cdot \mathbf{B} = 0.$$

After time-discretizatin, the field equations assume the following forms:

$$\begin{aligned} \mathbf{E}^{n+1} - \mathbf{E}^n &= c\,\Delta t\,\nabla \times \mathbf{B}^{n+\alpha} - 4\pi\,\Delta t\,\mathbf{j}^{n+\gamma}, \\ \mathbf{B}^{n+1} - \mathbf{B}^n &= -c\,\Delta t\,\nabla \times \mathbf{E}^{n+\alpha}. \end{aligned} \tag{6}$$

The electric and magnetic fields are defined on the same integer time level in Eq. (6). By using a linear interpolation of $\mathbf{B}^{n+\alpha} = \alpha \mathbf{B}^{n+1} + (1-\alpha)\,\mathbf{B}^n$, Eq. (6) is rewritten into

$$\begin{aligned} [1 + (\alpha c\,\Delta t)^2\,\nabla \times \nabla \times\,]\,\mathbf{E}^{n+1} &= [1 - \alpha(1-\alpha)(c\,\Delta t)^2\,\nabla \times \nabla \times\,]\,\mathbf{E}^n \\ &\quad + c\,\Delta t\,\nabla \times \mathbf{B}^n - 4\pi\,\Delta t\,\mathbf{j}^{n+\gamma}, \\ \mathbf{B}^{n+1} &= \mathbf{B}^n - c\,\Delta t\,\nabla \times [\alpha \mathbf{E}^{n+1} + (1-\alpha)\,\mathbf{E}^n]. \end{aligned} \tag{7}$$

Other two equations of the Maxwell equations appear as the initial condition to the electromagnetic field:

$$\nabla \cdot \mathbf{E}^0 = 4\pi q^0, \qquad \nabla \cdot B^0 = 0. \tag{8}$$

Actually, however, a correction to the longitudinal part of the electric field is required in particle simulations since q and $\mathbf{j}$ defined on the discrete grid points do not strictly satisfy the continuity equation [15]. The Gauss equation

$$\nabla \cdot \mathbf{E}^{n+1} = 4\pi q^{n+1} \tag{9}$$

is supplemented to Eqs. (7), (8). If we use a scalar potential $\delta\phi$, such that the final electric field $\mathbf{E}$ is given by $\mathbf{E} = \tilde{\mathbf{E}} - \nabla\delta\phi$, where $\tilde{\mathbf{E}}$ is the solution to Eq. (7), then Eq. (9) is rewritten into

$$-\nabla^2\,\delta\phi = 4\pi q^{n+1} - \nabla \cdot \tilde{\mathbf{E}}^{n+1}. \tag{10}$$

The current and charge densities appearing in Eqs. (7)–(10) are defined as summation over the particles, i.e., $\mathbf{j} = \sum e_j \mathbf{v}_j S(\mathbf{x} - \mathbf{x}_j)$, $q = \sum e_j S(\mathbf{x} - \mathbf{x}_j)$, where $\mathbf{S}(\mathbf{x})$ is a *shape function* to assign particle (Lagrangean) quantity to the neighboring field (Eulerian) grids. In order to make the whole equations implicit, i.e., stable for a large time step Δt, these current and charge densities must be expressed in terms of

the future electromagnetic fields $\mathbf{E}^{n+1}$, $\mathbf{B}^{n+1}$, and other known quantities with the aid of the equations of motion, Eqs. (3), (4):

$$\begin{aligned}\mathbf{j}^{n+\gamma}(\mathbf{x}) &= \sum e_j \mathbf{v}_j^{n+\gamma} S(\mathbf{x}-\tilde{\mathbf{x}}_j^{n+\gamma}) \\ &= \sum_i e_i \left[\mathbf{v}_j^n + \gamma\, \Delta t (e_i/m_i)(\mathbf{E}^{n+\alpha}(\tilde{\mathbf{x}}_j^{n+\gamma}) + \frac{\mathbf{v}^{n+1/2}}{c} \times \mathbf{B}^{n+\alpha}(\tilde{\mathbf{x}}_j^{n+\gamma}) \right] S(\mathbf{x}-\tilde{\mathbf{x}}_j^{n+\gamma}) \\ &\quad + \sum_e e[\mathbf{v}_\parallel^n + \gamma\, \Delta t (e/m_e)\, \mathbf{E}_\parallel^{n+\alpha}(\tilde{\mathbf{x}}_j^{n+\gamma}) + \mathbf{v}_\perp^{n+\gamma}(\tilde{\mathbf{x}}_j^{n+\gamma})]\, S(\mathbf{x}-\tilde{\mathbf{x}}_j^{n+\gamma}), \qquad (11)\end{aligned}$$

where the substitution $\mathbf{x}_j^{n+\gamma} \to \tilde{\mathbf{x}}_j^{n+\gamma} = \mathbf{x}_j^n + \gamma\, \Delta t\, \mathbf{v}_j^n$ has been done.

The charge density is expressed in somewhat a different manner for better stability of the scheme [16]. Namely, $\mathbf{x}_j^{n+1}$ is split into the known part $\mathbf{x}_l^{n+1}$ and a small displacement $\delta \mathbf{x}_j$ from it,

$$\begin{aligned}q^{n+1}(\mathbf{x}) &= \sum e_j S(\mathbf{x}-\mathbf{x}_j^{n+1}) \\ &= \sum_{i,e} e_j S(\mathbf{x}-\mathbf{x}_l^{n+1}) - \nabla \cdot \sum_{i,e} e_j \delta \mathbf{x}_j S(\mathbf{x}-\mathbf{x}_l^{n+1}), \qquad (12)\end{aligned}$$

which is derived by using the continuity of charge density. In Eq. (12), $\mathbf{x}_l^{n+1}$ is the sum of terms excluding $\mathbf{E}^{n+1}$, $\mathbf{B}^{n+1}$ dependent terms from $\mathbf{x}_j^{n+1}$,

$$\begin{aligned}\mathbf{x}^{n+1} &= \mathbf{x}^n + \mathbf{v}^{n+1/2}\, \Delta t \\ &= \mathbf{x}^n + \mathbf{v}^n\, \Delta t + \frac{1}{2} \Delta t^2 \frac{e_i}{m_i} \left[\mathbf{E}^{n+\alpha}(\tilde{\mathbf{x}}^{n+\gamma}) + \frac{\mathbf{v}^{n+1/2}}{c} \times \mathbf{B}^{n+\alpha}(\tilde{\mathbf{x}}^{n+\gamma}) \right] \\ &= \mathbf{x}^n + \mathbf{v}^n \Delta t + \frac{1}{2} \Delta t^2 \frac{e_i}{m_i} \left[\mathbf{E}^n(\tilde{\mathbf{x}}^{n+\gamma}) + \frac{\mathbf{v}^{n+1/2}}{c} \times \mathbf{B}^n(\tilde{\mathbf{x}}^{n+\gamma}) \right] + (\text{the rest}, \delta \mathbf{x}_j) \qquad (13)\end{aligned}$$

for the ions, and

$$\begin{aligned}\mathbf{x}^{n+1} &= \mathbf{x}^n + (\mathbf{v}_\parallel^{n+1/2} + \mathbf{v}_\perp^{n+\gamma})\, \Delta t \\ &= \mathbf{x}^n + (\mathbf{v}_\parallel^n + \mathbf{v}_\perp^n)\, \Delta t + \frac{1}{2} \Delta t^2 \frac{e}{m_e} \mathbf{E}_\parallel^{n+\alpha}(\tilde{\mathbf{x}}^{n+\gamma}) + \gamma\, \Delta t (\mathbf{v}_\perp^{n+1} - \mathbf{v}_\perp^n) \\ &= \mathbf{x}^n + (\mathbf{v}_\parallel^n + \mathbf{v}_\perp^n)\, \Delta t + \frac{1}{2} \Delta t^2 \frac{e}{m_e} \mathbf{E}_\parallel^n(\tilde{\mathbf{x}}^{n+\gamma}) - \gamma\, \Delta t\, \mathbf{v}_\perp^n + (\text{the rest}, \delta \mathbf{x}_j) \qquad (14)\end{aligned}$$

for the electrons.

Equations (7), (8), (10) together with Eqs. (11)–(14) form a closed set of equations. Once the future electromagnetic fields $\mathbf{E}^{n+1}$ and $\mathbf{B}^{n+1}$ are determined, the particle velocity and position are advanced using Eqs. (3) and (4). As is generally the case with implicit schemes, the backward-shifted algorithm tends to

suppress high frequency waves with $\omega \Delta t > 1$ and properly reproduces other low frequency waves (see Section 3). When we set $\alpha = \gamma = 1$, a fully backward algorithm is obtained. However, for better accuracy, $\alpha = \gamma \approx 0.6$ are normally chosen. These properties will be analytically proven in Section 3, and numerically verified in Section 4.

To solve the field–particle coupled equations described in this section, some iterations are required since there appear unknown electromagnetic fields $\mathbf{E}^{n+1}$ and $\mathbf{B}^{n+1}$ in the equations. In order to have a better convergence of the iteration, the major part of $\mathbf{j}^{n+\gamma}$ in the right-hand side of Eq. (7) is subtracted from both sides of the equation. Also the same procedure is executed to iteratively solve Eq. (10). These procedures greatly help a convergence of the iterations. Another significant improvement is made in the summation appearing in Eqs. (11) and (12) to increase accuracy and to minimize the time-consuming summation through the particle list. Namely,

$$\begin{aligned}
&\sum e_j \mathbf{E}^{n+\alpha}(\tilde{\mathbf{x}}_j^{n+\gamma})\, S(\mathbf{x} - \tilde{\mathbf{x}}_j^{n+\gamma}) \\
&\quad = \sum e_j \mathbf{E}^{n}(\tilde{\mathbf{x}}_j^{n+\gamma})\, S(\mathbf{x} - \tilde{\mathbf{x}}_j^{n+\gamma}) + \sum e_j \alpha(\mathbf{E}^{n+1} - \mathbf{E}^{n})(\tilde{\mathbf{x}}_j^{n+\gamma})\, S(\mathbf{x} - \tilde{\mathbf{x}}_j^{n+\gamma}) \\
&\quad = \sum e_j \mathbf{E}^{n}(\tilde{\mathbf{x}}_j^{n+\gamma})\, S(\mathbf{x} - \tilde{\mathbf{x}}_j^{n+\gamma}) + \alpha(\mathbf{E}^{n+1} - \mathbf{E}^{n})(\mathbf{x})\, q^{n+\gamma}(\mathbf{x}). \qquad (15)
\end{aligned}$$

Then the summation through the particle list is calculated essentially only once in each time step. Moreover, only several field iterations are necessary to solve Eqs. (7) and (10) for the accuracy of one percent in the electromagnetic fields. An operation per time step costs about three times more for this implicit scheme than for the semi-implicit predictor-corrector scheme [1, 2]. However, the choice of a large time step in the implicit algorithm easily compensates costly operations in each time step and enables us to do a far more efficient simulation (typically, one order less computation time for the same physics results). For the examples to be shown in Section 4, the run with both 32,000 electrons and ions, 32×64 cells takes only 3.5 s per time step on VP-200 (Fujitsu) computer.

3. Analytical Properties of Macroscale Particle Simulation Code

High frequency electrostatic oscillations that one is not interested in for global scale simulations arise from the finite electron inertia. To prove numerical stability of the electrostatic part of Eq. (7) [Eq. (9)], the Vlasov–Poisson equations for an infinite plasma are analyzed. The Vlasov equation is given by $\partial f^{n+1/2}/\partial t + \mathbf{v} \cdot \partial f/\partial \mathbf{x} + (e_j/m_j)(\mathbf{E}^{n+\alpha} + (\mathbf{v}/c) \times \mathbf{B}_0) \cdot \partial f_0/\partial \mathbf{v} = 0$, where the ambient magnetic field points the z-direction [unmagnetized ions are assumed]. Linearizing and integrating the equation along the orbit of characteristics by assuming the plane

wave solution $\mathbf{E}=\mathbf{E}_k \exp[i(\mathbf{k}\cdot\mathbf{x}-\omega t)]$ and the Maxwell distribution function f_0 for the electrons, yields the perturbed electron distribution function,

$$f_{ke}^{n+1/2}(\mathbf{v}_\parallel, \mathbf{v}_\perp, \psi)$$
$$= -(2e/m_e v_e^2) f_0 E_k^{n+\alpha} \sum_n (n\omega_{ce} + k_z v_z) J_n(\xi) \exp(i(n\psi - \sin\psi))$$
$$\div (\omega \sin\varepsilon/\varepsilon - n\omega_{ce} - k_z v_z), \tag{16}$$

where $\omega_{ce}=eB_0/m_e c$ and $v_e=(2T_e/m_e)^{1/2}$, respectively, are the cyclotron frequency and the thermal speed of the electrons, $\xi=k_x v_x/\omega_{ce}$ and $\varepsilon=\frac{1}{2}\omega\,\Delta t$. The $\sin\varepsilon/\varepsilon$ factor arises from the time derivative term $\partial f^{n+1/2}/\partial t=(f^{n+1}-f^n)/\Delta t \to f_{ke}^n[\exp(-i\omega\,\Delta t)-1]=-i\omega(\sin\varepsilon/\varepsilon) f_{ke}^{n+1/2}$. By subsituting f_{ke} and the unmagnetized ion perturbed distribution f_{ki} into Eq. (9), we have

$$E_k^{n+\alpha+1/2}/E_k^{n+1} = \exp(-i(\alpha-\tfrac{1}{2})\,\omega\,\Delta t)$$
$$= -1\Big/\Big((2\omega_{pe}^2/k^2v_e^2)\Big[1+\sum \xi_{e0} Z(\xi_{en})\, I_n(\mu)\, e^{-\mu}\Big]$$
$$+ (2\omega_{pi}^2/k^2 v_i^2)[1+\xi_i Z(\xi_i)]\Big), \tag{17}$$

where $\xi_{en}=((\sin\varepsilon/\varepsilon)\,\omega - n\omega_{ce})/k_z v_e$, $\mu=(k_x v_e)^2/2\omega_{ce}^2$, $\xi_i=(\sin\varepsilon/\varepsilon)\,\omega/kv_i$, and $Z(\xi)$ is the plasma dispersion function. Equation (17) gives a stability criterion of the *macroscale particle simulation code* against electrostatic waves.

Figure 1 shows a solution ω to Eq. (17) versus Δt for the Langmuir wave of the given wavenumber $\mathbf{k}=k\hat{z}$, $T_e/T_i=1$, and the decentering parameter $\alpha=0.6$. The complex root of Eq. (17) is almost independent of the wavenumber (as expected), and the Langmuir wave is recovered in the $\omega_{pe}\,\Delta t \to 0$ limit. For the finite time step Δt, the real part $\omega_r=\mathrm{Re}(\omega)$ of the solution first peaks at $\omega_{pe}\,\Delta t \approx 2$ and then decreases with $\omega_{pe}\,\Delta t$. The damping increment $|\omega_i|$ ($\omega_i=\mathrm{Im}(\omega)$) is found to peak

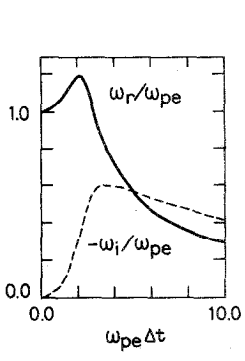

FIG. 1. The frequency ω_r (solid line) and the damping increment $|\omega_i|$ (dashed line) of the Langmuir wave ($\mathbf{k}/\!/\mathbf{B}_0$) versus time step Δt under the time-decentered scheme Eq. (9). The parameters are $k\lambda_e=0.1/\sqrt{2}$, $T_e/T_i=1$, and $\alpha=0.6$.

at $\omega_{pe}\,\Delta t \approx 4$ and it slowly decreases for $\omega_{pe}\,\Delta t > 4$. The damping factor $\exp(-|\omega_i|\,\Delta t)$ per time step is always much smaller than unity. Therefore, even for a choice of small (backward) decentering parameter α, the Langmuir wave is suppressed immediately for arbitrary Δt (>1) value.

The damping increment is easily obtained for the Langmuir wave and the upper hybrid wave in the cold electron limit ($v_e \to 0$). In this limit we have $E_k^{n+\alpha+1/2}/E_k^{n+1} = ((\omega \sin \varepsilon/\varepsilon)^2 - \omega_{ce}^2)/\omega_{pe}^2 = \exp(-i(\alpha - \frac{1}{2})\,\omega\,\Delta t)$. Expanding the exponential term assuming $(\alpha - \frac{1}{2})\,\omega\,\Delta t \ll 1$ yields $\omega_r^2 \approx \omega_{pe}^2 + \omega_{ce}^2$ and $\omega_i \approx -(\alpha - \frac{1}{2})\,\omega_{pe}\,\Delta t/2$.

The ion acoustic wave, on the other hand, is accurately reproduced by the present scheme when the time step is chosen small so that the wave frequency satisfies $\omega\,\Delta t < 1$. When $\omega\,\Delta t \ll 1$, the imaginary part of the solution to Eq. (17) is negative, $\omega_i/\omega_r \approx -0.06$, due to Landau damping ($T_e/T_i = 10$). The damping increment $|\omega_i|$ starts increasing slowly by artificial damping as the time step increases. When the time step becomes large so that $\omega\,\Delta t \approx 1$, the increase in the damping increment is still 20%. The change in the frequency is small for this time step because the denominator of Eq. (17) is a large quantity. It is concluded that the present scheme with the choice of $\omega_{pe}\,\Delta t > 1$ damps high frequency electrostatic waves and yet retains the low frequency waves.

Stability of Eq. (7) against the decentering of the current density is examined before its wave properties are analyzed. For the simplest and most interesting case, we use the electric $\mathbf{E} \times \mathbf{B}$ current assuming immovable ions, $\mathbf{j} = en_0 c\mathbf{E} \times \mathbf{B}_0/B_0^2$. For a plane wave solution $\mathbf{E}$, $\mathbf{B} = \mathbf{E}_k$, $\mathbf{B}_k \exp(-i(k_z z - \omega t))$, we have

$$\frac{c^2k^2}{\omega^2} \exp\left(-2i\left(\alpha - \frac{1}{2}\right)\omega\,\Delta t\right) - 1 \pm \frac{\omega_{pe}^2}{\omega\omega_{ce}} \exp\left(-i\left(\gamma - \frac{1}{2}\right)\omega\,\Delta t\right) = 0. \tag{18}$$

The solution to Eq. (18) for $ck/\omega_{pe} < 1$ and $\omega_{ce}/\omega_{pe} \approx 1$ is insensitive to α and is given by $\omega_r \approx \pm\omega_{pe}^2/\omega_{ce}$, $\omega_i \approx -(\omega_{pe}^2/\omega_{ce})^2\,(\gamma - \frac{1}{2})\,\Delta t$. Therefore, the choice of $\gamma > \frac{1}{2}$ makes the scheme Eq. (7) stable against the electron $\mathbf{E} \times \mathbf{B}$ drift current. In vacuum, Eq. (18) has a solution $\omega_r = \pm ck$ and $\omega_i = -c^2k^2(\alpha - \frac{1}{2})\,\Delta t$. Choice of $\alpha > \frac{1}{2}$ always makes Eq. (7) stable to the light wave.

The numerical property of the electromagnetic (magnetoinductive) part of Eq. (7) against waves is now analyzed. Assuming a plane wave solution, $\mathbf{E}$, $\mathbf{B} \approx \mathbf{E}_k$, $\mathbf{B}_k \exp[i(k_z z - \omega t)]$ yields

$$\begin{aligned}[1 + (\alpha ck\,\Delta t)^2]\,\mathbf{E}_{kT}^{n+1} = {} & [1 - \alpha(1-\alpha)(ck\,\Delta t)^2]\,\mathbf{E}_{kT}^{n} \\ & + i(c\,\Delta t)\,\mathbf{k} \times \mathbf{B}_k^n - 4\pi\,\Delta t\,\mathbf{j}_k^{n+\gamma},\end{aligned} \tag{19}$$

where $\mathbf{k} \cdot \mathbf{E}_{kT} = 0$. By expressing $\mathbf{B}_k^n$ in terms of $\mathbf{E}_{kT}^n$, we have

$$\begin{aligned}&[1 + (\alpha ck\,\Delta t)^2]\,\mathbf{E}_{kT}^{n+1} \\ &\quad = [1 - \alpha(1-\alpha)(ck\,\Delta t)^2 - i(c^2k^2/\tilde{\omega})\,\Delta t]\,\mathbf{E}_{kT}^{n} - 4\pi\,\Delta t\,\mathbf{j}_k^{n+\gamma},\end{aligned} \tag{20}$$

where $\tilde{\omega} = (\sin \varepsilon/\varepsilon)\,\omega$, $\varepsilon = (\frac{1}{2})\,\omega\,\Delta t$, and the relation $\mathbf{k} \times \mathbf{E}_{kT}^n = (\tilde{\omega}/c)\,\mathbf{B}_k^n$ has been utilized to relate $\mathbf{E}_{kT}^n$ with $\mathbf{B}_k^n$ of the same time level. The dispersion relation under the finite difference scheme Eq. (7) is obtained by equating $\mathbf{E}_k^{n+1}/\mathbf{E}_k^n$ with $\exp(-i\omega\,\Delta t)$.

The dispersion equation for high frequency electromagnetic waves propagating along the magnetic field $\mathbf{B}_0$ is obtained by substituting into Eq. (20) the electron current $\mathbf{j}_e = en_0(c/B_0)(\mathbf{E} \times \mathbf{B}_0/B_0 + i(\tilde{\omega}/\omega_{ce})\,\mathbf{E}_T)/(1 - \tilde{\omega}^2/\omega_{ce}^2)$ [17]. Then for $\alpha = \gamma = 1$, we have

$$[1 + (ck\,\Delta t)^2 - i\omega_{pe}\,\Delta t(\omega_{pe}/\omega_{ce})(-\tilde{\omega}/\omega_{ce} \pm 1)/(1 - \tilde{\omega}^2/\omega_{ce}^2)]\,E_{\pm}^{n+1} = [1 - i(c^2k^2/\tilde{\omega})\,\Delta t]\,E_{\pm}^n, \tag{21}$$

where $E_{\pm} = E_x \pm iE_y = E_k^{\pm} \exp(i(k_z z - \omega t))$. Equation (21) gives three stable circularly polarized electromagnetic wave branches [17] when $\Delta t = 0$, i.e., R mode ($\omega > \omega_R$), L mode ($\omega > \omega_L$), whistler mode (the lower R mode) [$\omega_{R,L} = \pm\,|\omega_{ce}| + (\omega_{pe}^2 + \omega_{ce}^2/4)^{1/2}$]. However, when the time step becomes finite $\omega_{pe}\,\Delta t > 1$, the first two branches become heavily damped because their frequencies are then comparable to $1/\Delta t$. The damping increment of the R and L modes when $\omega_{pe}\,\Delta t = 1$ are, respectively, $|\omega_i| \approx 0.30\omega_{pe}$ and $0.16\omega_{pe}$ at $ck_z/\omega_{pe} = 0.1$ ($\omega_{ce}/\omega_{pe} = 1$). On the other hand, the dispersion property of the whistler mode is not much altered compared to the theoretical one as far as $\omega\,\Delta t < 1$ is satisfied. The damping increment of the whistler mode is comparatively small, for example, $\omega/\omega_{pe} \approx 0.23 - 6 \times 10^{-3} i$ at $ck_z/\omega_{pe} = 0.5$.

The dispersion relation of the Alfven wave is properly reproduced. For this, the fluid equation is utilized to determine the current density:

$$m_i n(\mathbf{v}_i^{n+1} - \mathbf{v}_i^n)/\Delta t = (1/c)\,\mathbf{j}^{n+\gamma} \times \mathbf{B}_0, \qquad \mathbf{E} + (1/c)\,\mathbf{v}_i \times \mathbf{B}_0 = 0. \tag{22}$$

Solving Eq. (22) for $\mathbf{j}$ yields the ion polarization current, $\mathbf{j}^{n+\gamma} = (1/4\pi)(c/v_A)^2 \times (\mathbf{E}^{n+1} - \mathbf{E}^n)/\Delta t$, where $v_A = B_0/(4\pi m_i n)^{1/2}$ is the Alfven speed. Substituting Fourier transformed $\mathbf{j}_k^{n+\gamma} = (1/4\pi)(c/v_A)^2\,(-i\tilde{\omega})\,\mathbf{E}_k^{n+1/2}$ into Eq. (20) finally yields

$$\left[1 + (\alpha ck\,\Delta t)^2 - i\frac{\tilde{\omega}\,\Delta t}{2}(c/v_A)^2\right]\mathbf{E}_{kT}^{n+1} = \left[1 - \alpha(1-\alpha)(ck\,\Delta t)^2 - i\frac{c^2k^2}{\tilde{\omega}}\,\Delta t + i\frac{\tilde{\omega}\,\Delta t}{2}(c/v_A)^2\right]\mathbf{E}_{kT}^n. \tag{23}$$

The dispersion relation of the Alfven wave under the present scheme is finally obtained by substituting the wave form into Eq. (23).

The real and imaginary parts of the solution to Eq. (23) are plotted versus the time step in Fig. 2. The chosen parameters are $ck/\omega_{pe} = 0.01$, $v_A/c = 0.1$, and the decentering parameter is $\alpha = 0.6$. The frequency stays virtually at the same value

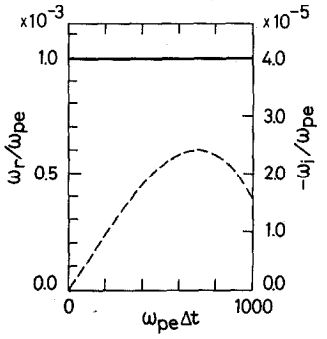

FIG. 2. The frequency ω_r (solid line) and the damping increment $|\omega_i|$ (dashed line) of the Alfven wave versus time step Δt under the time-decentered scheme Eq. (7). The parameters are $ck/\omega_{pe}=0.01$, $v_A/c=0.1$, and $\alpha=0.6$.

$\omega_r(\Delta t=0)$ between $\omega_{pe}\Delta t=0$ and 1000. The damping increment increases linearly with the time step and peaks at $\omega_{pe}\Delta t=700$. If we choose a fairly large time step $\omega_{pe}\Delta t=100$, i.e., $\omega\Delta t\approx 0.1$, the ratio of the damping increment to the frequency becomes $\omega_i/\omega_r\approx -4.9\times 10^{-3}$; $-e$ folding time of the wave amplitude is then 32.2 wave periods. When we choose the larger decentering parameter $\alpha=1.0$, we have $\omega_i/\omega_r\approx -0.025$ for $\omega_{pe}\Delta t=100$ and the $-e$ folding time becomes 6.4 wave periods. Therefore, it is stated that the time-decentered (backward) scheme Eq. (7) with a choice of the small decentering parameter, say $\alpha=\gamma=0.6$, is adequate to deal with low frequency electromagnetic phenomena with $\omega\Delta t\ll 1$.

4. Numerical Examples of Macroscale Particle Simulation

Two types of *macroscale particle simulation* are described in this section to numerically verify the properties discussed in Sections 2 and 3. As the first example, electromagnetic eigenmodes in a 2D magnetized thermally equilibrium plasma are examined. As the second one, a propagation and damping of the finite amplitude kinetic Alfven wave is described.

4a. *Analysis of Thermal Plasma Eigenmodes*

As an initial condition a homogeneous, thermally near-equilibrium plasma is prepared by quiet start technique with $T_e/T_i=10$, $\omega_{ce}/\omega_{pe}=1$, the electron beta $\beta_e=0.09$ and $m_i/m_e=100$. A two-dimensional (x, z) periodic system of 32×64 cells is used with the system length $L_x=200c/\omega_{pe}$ and $L_z=400c/\omega_{pe}$ (the ambient magnetic field points the z-direction). At the initial loading, approximately 15 electrons and ions are put in each cell. Time step of $\Delta t=20\omega_{pe}^{-1}$ is used in this section to follow the ion cyclotron motion correctly ($\omega_{ci}\Delta t=0.2$). The electromagnetic fields are normalized as $\hat{\mathbf{E}}=e\mathbf{E}/m_e c\omega_{pe}$, $\hat{\mathbf{B}}=e\mathbf{B}/m_e c\omega_{pe}$, and the scalar potential field as $\hat{\phi}=e\phi/m_e c^2$. A power spectrum analysis is performed using the maximum

entropy method [18]. The data span used for this analysis is $\approx 10000\omega_{pe}^{-1}$ or $100\omega_{ci}^{-1}$. The same run has been used for the spectrum analysis of Figs. 3 to 6; Figs. 3 and 6 show the spectra for the fixed value of $ck_x/\omega_{pe} = 2\pi/L_x$; Figs. 4 and 5 show those for the fixed value of $ck_z/\omega_{pe} = 2\pi/L_z$.

Shown in Fig. 3 is the Fourier amplitude of the magnetic field $\mathbf{B}_y(\omega, k_z)$ [k_x is fixed as stated above]. In the figure, the abscissa is the wavenumber ck_z/ω_{pe}, the ordinate the frequency ω/ω_{pe}, and the Fourier amplitude $\mathbf{B}_{ky}$ is plotted on a logarithmic scale (10^4 range) above (to the right of) discrete baselines. The Fourier amplitude in the figure shows two series of distinct peaks. One branch extending up to the frequency higher than ω_{ci} corresponds to the whistler mode (lower R mode). The other branch that approaches $\omega \to \omega_{ci}$ ($=0.01\omega_{pe}$) at the large wavenumber k_z corresponds to the Alfven wave mode (lower L mode). The same spectra (mode branches) are also found in the $\mathbf{E}_x$, $\mathbf{E}_y$, and $\mathbf{B}_x$ fields for the nearly parallel propagation.

The theoretical dispersion relation for both branches are superimposed in Fig. 3 by the solid (Alfven) and dashed (whistler) lines. The agreement between the measured dispersion of the simulation and that of the theory is excellent. (Note that the frequency value must be read by projecting the peaks onto the baseline.) Here in the theoretical dispersion relation, the finite size particle effect is included. The whistler branch in Fig. 3 extends up to $\omega/\omega_{pe} \approx 0.05$ and disappears above it. This is caused by an artificial damping due to the time (and partly spatial) filtering. It is notable that high frequency eigenmodes much above $\omega \approx 1/\Delta t$, such as the R, L modes, are not detected.

The power spectrum of the magnetic field $\mathbf{B}_z(\omega, k_x)$ for the nearly perpendicular propagation in Fig. 4 shows a distinct branch that goes up through $\omega \approx \omega_{ci}$. This corresponds to the fast magnetosonic wave whose theoretical dispersion relation is

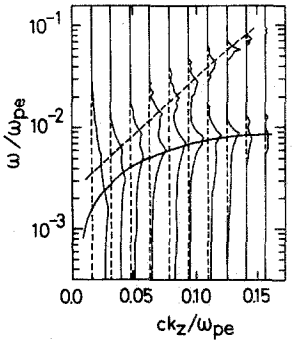

FIG. 3. The power spectrum of the magnetic field $\mathbf{B}_y(\omega, k_z)$ in a thermal equilibrium plasma. The spectrum is shown as a function of the frequency ω/ω_{pe} and the discrete value of the parallel wavenumber ck_z/ω_{pe} (corresponding to the vertical baselines) for the fixed value of ck_x/ω_{pe} ($=2\pi/L_x$). Above (i.e., to the right of) each baseline, the Fourier amplitude is plotted on a logarithmic scale such that the increment between the baselines is 10^4. The solid and dashed lines are the theoretical dispersion relations for the Alfven and whistler waves, respectively.

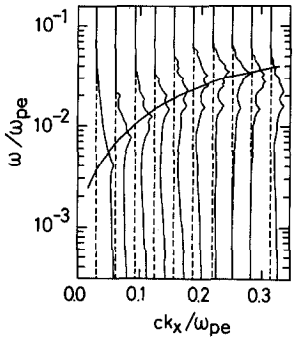

FIG. 4. The power spectrum of the magnetic field $\mathbf{B}_z(\omega, k_x)$ for the same run as in Fig. 3, except the abscissa is now the perpendicular wavenumber ck_x/ω_{pe} and that $ck_z/\omega_{pe} = 2\pi/L_z$ is fixed. The solid line in the figure shows the theoretical dispersion relation of the fast magnetosonic wave.

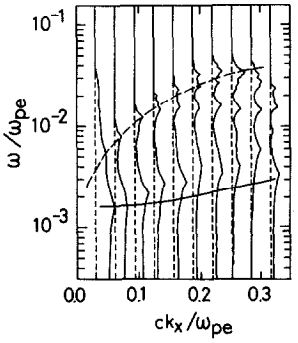

FIG. 5. The power spectrum of the magnetic field $\mathbf{B}_y(\omega, k_x)$ as a function of the frequency ω/ω_{pe} and the perpendicular wavenumber ck_x/ω_{pe} for the fixed value of ck_z/ω_{pe} $(=2\pi/L_z)$. The lower frequency eigenmode is the kinetic Alfven wave branch and the upper eigenmode the fast magnetosonic wave branch.

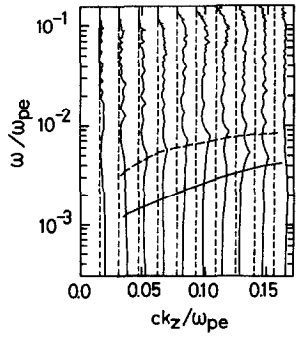

FIG. 6. The power spectrum of the electric field $\mathbf{E}_z(\omega, k_z)$ for the nearly parallel propagation with $ck_x/\omega_{pe} = 2\pi/L_x$ being fixed.

shown by the solid line in the figure. The magnetosonic branch is also found in the $\mathbf{E}_y$ field. On the other hand, the $\mathbf{B}_y(\omega, k_x)$ magnetic field of Fig. 5 has an eigenmode at the low frequency $\omega \approx 2 \times 10^{-3} \omega_{pe}$ which is the kinetic Alfven wave branch [19]; its dispersion relation is given by

$$\omega \approx k_z v_A \left[1 + \left(\frac{3}{4} + \frac{T_e}{T_i} \right) k_x^2 \rho_i^2 \right], \tag{24}$$

where ρ_i is the ion Larmor radius. An exact theoretical dispersion relation is calculated and plotted by the solid line in the figure. The same result was previously obtained by the semi-implicit algorithm (Fig. 1 of Ref. [2]). The other smaller peaks extending above $\omega \approx \omega_{ci}$ corresponds to the magnetosonic branch. These two branches are also found in the $\mathbf{E}_x$ electric field. But, the kinetic Alfven wave branch is absent in the $\mathbf{E}_y$, $\mathbf{B}_z$ fields. The linear wave analysis supports these observations; the ratio of the Fourier amplitude is $|B_{kz}/B_{ky}| \approx 5.5$ for the magnetosonic branch and $|B_{kz}/B_{ky}| \ll 1$ for the kinetic Alfven branch at $ck_x/\omega_{pe} = 0.16$ and $ck_z/\omega_{pe} = 2\pi/L_z$. There observed no eigenmode in the $\mathbf{B}_y$ field above $\omega \approx 0.05\omega_{pe}$, showing absence of the O mode ($\omega \approx \omega_{pe}$) due to the choice of the large time step, $\omega_{pe} \Delta t = 20$. The X mode is not observed in the $\mathbf{B}_z$ field, either.

As expected from the linear analysis of the electrostatic waves in Section 3 under the backward scheme Eq. (9), no eigenmode is found above $\omega \approx 0.1\omega_{pe}$ in the $\mathbf{E}_z$ electric field for the parallel propagation of Fig. 6. The Fourier amplitude of the $\mathbf{E}_z$ field is by two orders of magnitude smaller than that of the $\mathbf{E}_x$ field in the same run. The lower faint peaks present at the middle of the broad plateau $\omega < \omega_{ci}$ correspond to the ion acoustic wave. The upper peaks which are less damped by linear wave analysis are also observed. Theoretical dispersion relations are shown with the solid lines in the figure. The faintness and broadness of these modes may be due to damping of the mode branches under the given parameters.

4b. *Propagation and Damping of Kinetic Alfven Wave*

The kinetic Alfven wave is the Alfven wave for which wave–particle interactions are important [19]. This wave propagates almost perpendicularly to the ambient magnetic field $\mathbf{B}_{0z}$ since $k_z \ll k_x \approx \rho_i^{-1}$. Also this wave is heavily Landau damped due to its parallel electric field.

In this simulation, a two-dimensional periodic system with 32×64 cells is used with $L_x = 50c/\omega_{pe}$ and $L_z = 400c/\omega_{pe}$. The plasma parameters are $T_i/T_e = 4$, $\beta = 0.26$, $\omega_{pe}/\omega_{ce} = 1$, and $m_i/m_e = 50$. Then the ion Larmor radius is $\rho_i = 2.1c/\omega_{pe}$

and to trace the ion cyclotron motion, i.e., $\omega_{ci} \Delta t = 0.4$. At the beginning of the simulation run, finite amplitude kinetic Alfven wave (monochromatic) is loaded in terms of charge and current density perturbations into a thermally quiet plasma with the wave mode number $n_x = n_z = 1$ ($ck_x/\omega_{pe} \approx 0.13$, $ck_z/\omega_{pe} \approx 0.016$). This corresponds to $k_x \rho_i \approx 0.38$. (For the details of the physics results, refer to Ref. [2]).

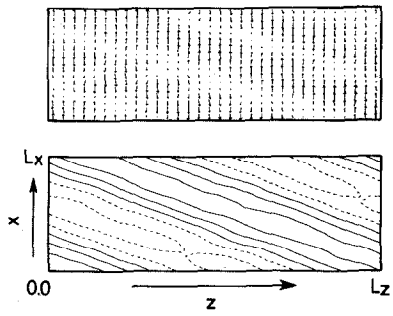

FIG. 7. The $(\mathbf{E}_x, \mathbf{E}_z)$ electric field and the $\mathbf{B}_y$ magnetic field of the kinetic Alfven wave at time $t/\tau_A = 2.8$.

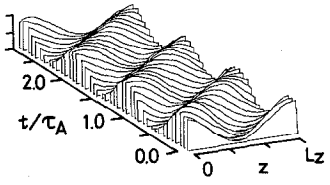

FIG. 8. The propagation of the kinetic Alfven wave is shown for the magnetic field $\mathbf{B}_y(z, t; x)$ (sliced at constant $x-$coordinate) between $t/\tau_A = 0$ and 2.8. The initial sinusoidal wave form is well preserved with a physical damping of the wave.

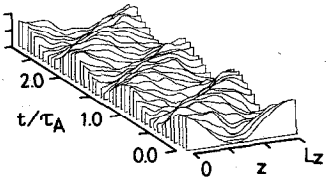

FIG. 9. The same as Fig. 8 except that the electric field $\mathbf{E}_x(z, t; x)$ is shown here.

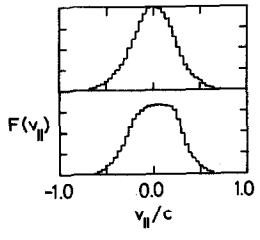

FIG. 10. The electron distribution function parallel to the ambient magnetic field for $t/\tau_A = 0$ and 1.4.

The amplitude of the initially loaded wave is about 15% of the ambient magnetic field.

Shown in Fig. 7 are the $(\mathbf{E}_x, \mathbf{E}_z)$ electric field and the $\mathbf{B}_y$ magnetic field at $t/\tau_A = 2.8$, where $\tau_A = 2\pi/k_z v_A$ is the Alfven wave period. The major electric field is the $\mathbf{E}_x$ field ($\mathbf{E}_x < 3 \times 10^{-2}$) and the $\mathbf{B}_y$ field ($\mathbf{B}_y < 0.14$). The loaded wave propagates quite obliquely to the ambient magnetic field. The propagation of the kinetic Alfven wave is clearly shown in the bird's-eye-view plot of Fig. 8, where the magnetic field $\mathbf{B}_y(z, t; x)$ is plotted for the fixed x-coordinate up to $t/\tau_A \approx 2.8$. The initially loaded sinusoidal kinetic Alfven wave is found to propagate nicely keeping the initial wave form. The $\mathbf{E}_x$ electric field in Fig. 9, which consists of almost the space charge field (hence noisy compared to the $\mathbf{B}_y$ field), always keeps the same phase with the $\mathbf{B}_y$ field.

As noted earlier in this section, the kinetic Alfven wave is subject to Landau damping. The damping increment $|\omega_i|$ is measured from the decrease in the wave magnetic energy which quite well follows $\exp(-2|\omega_i| t)$. The measured frequency and the damping increment are $\omega/k_z v_A = 1.08 - 1.6 \times 10^{-2} i$. The theory of the kinetic Alfven wave gives $\omega_{th}/k_z v_A = 1.10 - 1.4 \times 10^{-2} i$. The agreement is almost complete. Associated with the wave damping, heating of the plasma is detected. Shown in Fig. 10 is the electron velocity distribution function parallel to the ambient magnetic field. Flattening in the distribution function is observed at the velocity corresponding to the wave phase speed ($\omega/k_z \approx 0.15$). All these results are quite in good agreements with the previously obtained semi-implict simulation results [2].

The total energy of the present simulation system decreases slowly and monotonically due to the use of the *time-decentered* (*backward*) scheme. There occurs a small amplitude oscillation in the magnetic and electric field energy due to a slight mismatch in the initial wave loading. The period of this energy oscillation is exactly $\frac{1}{2}\tau_A$ which results from energy transfer between the wave and the particles (mainly ions). When the magnetic energy decreases, there occurs an increase in both the wave electric field energy and the particle kinetic energy, and vice versa. The decrease in the total energy (the field energy plus the kinetic energy) of the simulation system is within a percent up to three wave periods. On the other hand, we do not have any symptom of unphysical total energy increase that leads to blowup of the simulation run. This is one of the advantages of the *macroscale particle simulation code.*

5. Summary and Conclusion

A fully implicit and multi-dimensional electromagnetic particle simulation code—*macroscale particle simulation code*, was described in this paper. The field–particle coupled equations were derived in Section 2 using a complete set of the Maxwell equations and the equations of motion. The time-decentered dis-

cretization technique was made use of throughout the scheme to achieve large time and spatial scales compared to the electron characteristic time and spatial scales, i.e., ω_{ce}, ω_{pe}, and λ_e. A closed set of the field–particle coupled equations Eqs. (7), (8), (10) with Eqs. (11)–(14) was solved iteratively. Particles were advanced using Eqs. (3) and (4). The summation through the particle list could be minimized and only a few iterations (usually two) were necessary for the examples shown in Section 4. By virtue of the time-decentered (slightly backward) implicit algorithm, this simulation code was numerically stable and had an adequate numerical accuracy for the low frequency waves.

The advantages of the present simulation code were the following. First, the restriction on the time and spatial scales were relaxed to $\Delta x \gg \lambda_e$ and $\omega_{pe} \Delta t \gg 1$. Second, the decentered time differential algorithm which was used throughout the present scheme suppressed high frequency electrostatic and magnetoinductive waves; low frequency waves were proven to be properly reproduced. (See Sections 3 and 4 for the details.) An almost pure artificial damping of high frequency waves introduced by the backward time discretization in the *macroscale particle simulation code* made the nonlinear behavior of the plasma quite credible. Finally, in contrast to fluid codes, the use of the finite mass electrons enabled us to properly treat large-scale scalar potential electric field and the electron response to the slowly varying electromagnetic waves.

As a numerical verification of the scheme, two types of the 2D magnetized plasma simulations were performed. The eigenmodes in a thermal equilibrium plasma and the propagation of the finite amplitude kinetic Alfven wave were examined in Section 4. In the former simulation, low frequency eigenmodes such as the whistler wave, the Alfven wave, and the fast magnetosonic wave were shown to be properly reproduced, whereas high frequency eigenmodes were suppressed and were not detected. In the latter simulation, the initially loaded kinetic Alfven wave showed theoretically predicted frequency and damping, and its overall wave form was nicely preserved even after several wave periods. As a nonlinear phenomenon, the acceleration of the electrons was also observed. The distortion of the wave was even smaller for the fully implicit scheme than for the semi-implicit predictor-corrector scheme [2], probably due to damping of medium frequency waves (noise).

Before closing this paper, the proper way of applying the present particle simulation code is mentioned. As noted in Section 1, the present simulation code was developed to study global (MHD) scale kinetic behavior of magnetized plasmas. There are no a priori restrictions on the time step Δt and the grid interval Δx to the present scheme. This scheme is free from the Courant–Friedricks–Lewy condition since the field equations are implict. But, the restrictions on Δt and Δx arise from physical considerations. First, the time step and the grid interval must be small compared to the characteristic scales ω, L of the phenomena to be studied, i.e., $\omega \Delta t \ll 1$ and $\Delta x/L \ll 1$. Second, fast particles must not travel more than one wavelength within a time step to avoid appearance of a false force, i.e., $k_\parallel v \Delta t < 1$ must be satisfied where v is the fastest of the thermal and drift speeds of particles.

Third, if the ions are treated as magnetized species and their Larmor motion is traced, the time step must satisfy $\omega_{ci}\,\Delta t < 1$.

The following argument results from the aforementioned restrictions. The wavelength of some drift waves (e.g., the lower hybrid drift waves) is scaled by the electron Larmor radius ρ_e which can be close to the Debye length λ_e ($\rho_e/\lambda_e = \omega_{ce}/\omega_{pe}$) in nuclear fusion plasmas. Similarly, the wavelength of ion acoustic waves becomes $\approx \lambda_e$ when their frequency is close to the ion plasma frequency ω_{pi}. On the other hand, the wavelength of the Alfven wave of $\omega \approx \omega_{ci}$ is close to c/ω_{pi}. Since these two scale lengths are incompatible, one has to introduce theoretically derived or phenomenological collisions (if any) into the equations of motion to incorporate the transport effects associated with high frequency, minute scale turbulence.

As for the future plan, inclusion of plasma inhomogeneity and modification of the boundary conditions to other than the periodic condition and conducting walls, are the urgent problems. The extension of the code along this line is not difficult by virtue of a simple form of the field equations adopted in the present scheme, i.e., Eqs. (7) and (10). A torus effect (e.g., a tokamak) and ionization collisions may be also important for applications to some plasmas. Actually, these problems are now under study and will be reported in the future.

ACKNOWLEDGMENTS

The author is grateful to Dr. T. Sato who suggested him to develop the macroscale particle simulation code and provided him with valuable discussions. Constructive review by referees is also acknowledged. This work was supported by a Grant-in-Aid of the Ministry of Education, Sciences, and Culture of Japan.

REFERENCES

1. M. TANAKA AND T. SATO, *Phys. Fluids* **29**, 3823 (1986).
2. M. TANAKA, T. SATO, AND A. HASEGAWA, *Geophys. Res. Lett.* **14**, 868 (1987).
3. C. K. BIRDSALL AND A. B. LANGDON, *Plasma Physics via Computer Simulation* (McGraw–Hill, New York, 1983).
4. R. J. MASON, *J. Comput. Phys.* **41**, 233 (1981).
5. J. DENAVIT, *J. Comput. Phys.* **42**, 337 (1981).
6. J. U. BRACKBILL AND D. W. FORSLUND, *J. Comput. Phys.* **46**, 271 (1982).
7. D. W. FORSLUND AND J. U. BRACKBILL, *Phys. Rev. Lett.* **48**, 1614 (1982).
8. A. B. LANGDON, B. I. COHEN, AND A. FRIEDMAN, *J. Comput. Phys.* **51**, 107 (1983).
9. D. C. BARNES, T. KAMIMURA, J.-N. LEBOEUF, AND T. TAJIMA, *J. Comput. Phys.* **52**, 480 (1983).
10. T. KAMIMURA, T. TAJIMA, J. N. LEBOEUF, AND D. C. BARNES, *J. Comput. Phys.*, in press.
11. D. W. HEWETT, A. B. LANGDON, AND C. E. MAX, *Bull. Amer. Phys. Soc.* **31**, 1604 (1986).
12. M. TANAKA AND T. SATO, in *Proceedings International School for Space Simulation, Kauai, Hawaii*, 1985; Institute for Fusion Theory Report No. 117, Hiroshima University, 1986.

13. M. TANAKA, in *Proceedings*, 12th *Numerical Simulation Meeting, San Francisco*, 1987.
14. A. B. LANGDON AND D. C. BARNES, in *Multiple Time Scales*, edited by J. U. BRACKBILL AND B. I. COHEN, p. 335 (Academic Press, New York, 1985).
15. A. B. LANGDON AND B. F. LASINSKI, in *Methods Comput. Phys.* **16**, 327 (1976).
16. A. B. LANGDON, *J. Comput. Phys.* **30**, 202 (1979).
17. T. H. STIX, *The Theory of Plasma Waves* (McGraw–Hill, New York, 1962).
18. T. J. ULRYCH AND T. N. BISHOP, *Rev. Geophys.* **13**, 183 (1975); S. M. KAYE AND S. L. MARPLE, *Proc. IEEE* **69**, 1380 (1981).
19. A. HASEGAWA AND L. CHEN, *Phys. Fluids* **19**, 1924 (1976).